

Mapping glacier basal sliding applying machine learning

Josefine Umlauf¹, Christopher W. Johnson², Philippe Roux³, Daniel Taylor Trugman⁴, Albanne Lecointre³, Andrea Walpersdorf³, Ugo Nanni⁵, Florent Gimbert⁶, Bertrand Rouet-Leduc⁷, Claudia Hulbert⁸, Stefan Lüdtke⁹, Sascha Marton¹⁰, Paul A. Johnson²

¹ScaDS.AI - Center for Scalable Data Analytics and Artificial Intelligence, Leipzig University,

Humboldtstraße 25, 04105 Leipzig, Germany

²Los Alamos National Laboratory, Los Alamos, 87545, New Mexico, United States of America

³ISTerre - Institut des Sciences de la Terre, Maison des Geosciences, Rue du la Piscine 1383, Grenoble,

38041, France

⁴University of Nevada, Reno, Nevada Seismological Laboratory, N. Virginia Street, Reno, 1664, Nevada,

United States of America

⁵University of Oslo, Department of Geosciences, Sem Sælands vei 1, Oslo, 0371, Norway

⁶IGE - Institut de Geophysique de l'Environnement, Saint-Martin-d'Herès, Grenoble, 38400, France

⁷Disaster Prevention Research Center, Kyoto University, Gokasho, Uji, Kyoto, 611-0011, Japan

⁸Ecole Normale Supérieure, Paris, France

⁹Institute for Visual & Analytic Computing, University of Rostock

¹⁰Institute for Enterprise Systems, University of Mannheim

Key Points:

- Seismic and GPS data are examined to study physical processes controlling glacial basal motion
- Decision tree model uses beamforming catalog and statistical features of time series to constrain correlations with GPS recorded motions
- Glacial on-ice velocity is strongly modulated by activity at the base of the glacier

Corresponding author: Josefine Umlauf, josefine.umlauft@uni-leipzig.de

Abstract

During the RESOLVE project (“High-resolution imaging in subsurface geophysics: development of a multi-instrument platform for interdisciplinary research”), continuous surface displacement and seismic array observations were obtained on Glacier d’Argentière in the French Alps for 35 days in May 2018. The data set is used to perform a detailed study of targeted processes within the highly dynamic cryospheric environment. In particular, the physical processes controlling glacial basal motion are poorly understood and remain challenging to observe directly. Especially in the Alpine region for temperate based glaciers where the ice rapidly responds to changing climatic conditions and thus, processes are strongly intermittent in time and heterogeneous in space. Spatially dense seismic and GPS measurements are analyzed applying machine learning to gain insight into the processes controlling glacial motions of Glacier d’Argentière. Using multiple bandpass-filtered copies of the continuous seismic waveforms, we compute energy-based features, develop a matched field beamforming catalogue and include meteorological observations. Features describing the data are analyzed with a gradient boosting decision tree model to directly estimate the GPS displacements from the seismic noise. We posit that features of the seismic noise provide direct access to the dominant parameters that drive displacement on the highly variable and unsteady surface of the glacier. The machine learning model infers daily fluctuations and longer term trends. The results show on-ice displacement rates are strongly modulated by activity at the base of the glacier. The techniques presented provide a new approach to study glacial basal sliding and discover its full complexity.

Plain Language Summary

Alpine glaciers are a major component in the dynamic cryospheric environment. They are characterized by a multitude of processes occurring side by side, including but not limited to melt water flow, crevasse formation, and frictional basal sliding of the ice mass over the rigid and obstructive bedrock. Each of these processes generates distinctive acoustic signals that can be recorded by seismic instruments and the changing on-ice motions are resolvable with GPS. Considering the rapidly changing glacial environment, there is an increasing need for reliable models to predict glacial dynamics to properly assess any associated hazard. Understanding basal sliding is of particular interest to this problem. Investigated here is how to overcome the challenge of describing glacier sliding using

58 seismic signals since the records often contains multiple “loud” signals originating from
59 associated surface processes within the glacier. To uncover specific processes occurring at
60 the ice-bedrock interface, we design a machine learning model to incorporate signals
61 recorded on the glacier to predict the on-ice surface motions. The results provide valuable
62 insights into the spatiotemporal dynamics of an active Alpine glacier with the potential to
63 contribute to a better understanding of the driving mechanisms of glacier sliding.

64 **1 Introduction**

65 The cryosphere is one of the most rapidly changing environments on Earth and
66 transformations are accentuated by the ongoing evolution of climatic conditions. In
67 mountainous regions, glacier dynamics can be used as a local marker of climate change,
68 and can cause major damage to human infrastructure, so it is of common social interest
69 to study spatiotemporal processes within the ice with high resolution (Faillettaz et al.,
70 2015). The rapidly emerging field of “cryoseismology” addresses processes within the
71 glacial environment, such as crevassing, hydrofracturing, failure and calving of ice
72 fragments or supraglacial, englacial and subglacial water discharge via the analysis of
73 continuous seismic records (Podolskiy & Walter, 2016). Special emphasis has been put on
74 the investigation of glacier sliding, which is still not completely understood, but affects
75 large-scale ice flow, ice sheet stability, and thus ultimately sea level rise (Ritz et al., 2015).

76 Glaciers flow via two processes, internal deformation (or “creep”) and basal sliding
77 (Cuffey & Paterson, 2010). The stress-strain relationship for internal deformation of the
78 glacier itself describes viscous deformation associated with ice creep and can be
79 approximated by “Glen’s flow law” (Glen, 1955). Basal sliding is responsible for fast flow
80 of ice-streams; “sliding” is used as an umbrella term here for actual sliding of the ice sole
81 and deformation of soft subglacial till beds (e.g., Helanow et al., 2021). In view of steep,
82 unstable ice tongues, it is of great interest to scientists and stakeholders to understand the
83 physical basis of glacier sliding given that catastrophic break-off events threaten mountain
84 communities world-wide (Faillettaz et al., 2015; Shugar et al., 2021).

85 The first theoretical concept of glacier sliding was introduced by postulating that normal
86 forces on undeformable bed undulations produce local shear resistance (Weertman, 1957).
87 Here, a frictionless glacier bed was considered with sliding driven by enhanced
88 deformation and regelation around stiff bed obstacles. Weertman’s theory of “hard” bed

89 sliding (Weertman, 1957) was modified to account for subglacial water cavity formation
90 (Iken, 1981; Schoof, 2005; Gagliardini et al., 2007) and deformable subglacial till layers
91 (Murray, 1997). Both mechanisms can explain observations of melt-water enhanced ice
92 flow and basal sliding (Cuffey & Paterson, 2010). Modern sliding theories (e.g., Schoof,
93 2005; Zoet & Iverson, 2020) are still influenced by these concepts. However, recent
94 cryoseismological studies show that glacier sliding is not always smooth, but interrupted
95 by distinct slip events (Aster & Winberry, 2017). This points to frictional processes,
96 where sudden shear failure at the glacier bed emits seismic waves, analogous to the
97 behavior of tectonic faults. Such stick-slip motion cannot be explained by traditional
98 Weertman-type or soft-bed theories, which describe sliding as a continuous, slow, and
99 smooth process. Instead, frictional processes add to the complexity of basal sliding and
100 thus ice flow. A pivotal challenge in glaciological research is to formulate new or extend
101 existing sliding laws, including conventional concepts but also considering glacier frictional
102 sliding as an additional flow mechanism (e.g., Sergienko et al., 2009; Winberry et al.,
103 2011; Lipovsky & Dunham, 2017; Lipovsky et al., 2019; Zoet & Iverson, 2020).

104 Evidence from polar and non-polar ice masses suggests that microseismic stick-slip motion
105 is a widespread (see Podolskiy & Walter, 2016, and references therein) and potentially
106 pervasive form of basal sliding (Barcheck et al., 2019; Hudson et al., 2020; McBrearty et
107 al., 2020; Walter et al., 2020; Gräff et al., 2021; Kufner et al., 2021). Individual
108 microseismic stick-slip events are very small with negative magnitudes and shear
109 displacements on millimeter scales or less (Helmstetter et al., 2020). Successive events
110 may coalesce into sustained ice-tremor resulting in ice-stream wide sliding episodes with
111 surface displacements of tens of centimeters per day. The spectral signature of the sliding
112 tremor is characterized by spectral peaks at frequencies corresponding to the inverse of
113 inter-event times between individual stick-slip events (Lipovsky & Dunham, 2016). First
114 detected at rapid Antarctic ice streams, sliding tremor may be a widespread phenomenon
115 with observational evidence for these sliding tremors beneath Greenlandic (McBrearty et
116 al., 2020) and Alpine glacier ice (Umlauf et al., 2021), and the slip displacement may be
117 measurable at the ice surface. Detection of these tremors with conventional on-ice
118 seismometers is challenging because the signals can be masked by the extensive glacial
119 noise from other cryoseismic sources, especially englacial and subglacial water flow (Röösli
120 et al., 2014; McBrearty et al., 2020; Eibl et al., 2020; Umlauf et al., 2021). Thus, in
121 Alpine regions, with temperate glacier ice and high meltwater production, frictional

122 sliding in the form of microseismic stick-slip tremors may be completely overlooked and
123 far more predominant than presently understood.

124 Analogous to tectonic faults, stick slip motion across glacial faults emits seismic energy
125 and is commonly measured by seismometers (Podolskiy & Walter, 2016). The frictional
126 state of a tectonic fault and information about the current position within its seismic
127 cycle are still challenging to access. As the fault's rupture, nucleation and magnitude, and
128 future earthquake occurrence are directly controlled by the fault frictional state, its
129 quantification is of interest for understanding the underlying physics (Marone, 1998).
130 Numerous theoretical simulations and laboratory experiments contributed to the
131 determination of frictional characteristics (e.g., Rabinowicz, 1956; Scholz, 1968;
132 Rubinstein et al., 2004; Kaproth & Marone, 2013; Madariaga & Ruiz, 2016; Dorostkar et
133 al., 2017). Recently, analyses of seismic signals from laboratory faults (Rouet-LeDuc,
134 Hulbert, Bolton, et al., 2018) and faults in earth (Johnson & Johnson, 2021) applying
135 machine learning have yielded remarkable results indicating that the seismic waves
136 contain information about the fault characteristics at all times.

137 We use this analogy to guide the choice of research methodology to monitor the physical
138 state of the glacier. So far, direct and continuous quantification of fault friction cannot be
139 achieved using conventional geophysical approaches, whereas supervised machine learning
140 models are suitable to directly quantify instantaneous fault friction in laboratory
141 experiments and fault properties in tectonic environments (Rouet-LeDuc, Hulbert, Bolton,
142 et al., 2018; Rouet-LeDuc, Hulbert, & Johnson, 2018; Hulbert et al., 2019; Johnson &
143 Johnson, 2021; Ren et al., 2020; Wang et al., 2021, 2022).

144 In laboratory experiments it was demonstrated that frictional properties can be accessed
145 through the statistical characteristics of continuous seismic records (range of the data,
146 root mean square, variance, skewness, kurtosis, quantile ranges) and that even different
147 modes of slip along these laboratory faults were captured, which demonstrates that
148 seismic data are a rich archive that allows one to directly observe the physical state of a
149 fault (Rouet-LeDuc, Hulbert, Bolton, et al., 2018; Hulbert et al., 2019). These processes
150 are similar to basal motion in the glacial environment where the displacement takes place
151 at the ice-bed-interface.

152 With the aim to uncover the signals related to sliding that are not directly observable, we
153 applied a decision tree model to a new data set from a dense on-ice network on Glacier

154 d’Argentière (French Alps) comprising continuous measurements of local seismicity,
155 surface velocities, and meteorological observations. Due to the highly variable and noisy
156 glacial environment, extensive preprocessing of the seismic and geodetic measurements is
157 essential for a robust feature space with the goal of directly estimating glacier sliding
158 behavior from the surface of the ice and hence, to monitor its dynamics.

159 **2 Methods**

160 **2.1 Resolve data collection**

161 As part of the RESOLVE project “High-resolution imaging in subsurface geophysics:
162 development of a multi-instrument platform for interdisciplinary research”), researchers
163 from ISTERre and IGE Grenoble (France) and ETH Zürich (Switzerland) installed a
164 unique sensor infrastructure at the surface of Glacier d’Argentière (Fig. 1) (Gimbert et
165 al., 2021). A dense seismic monitoring array with 98 geophones, 7 GPS stations, a
166 meteorological station, and a water discharge station were operational during
167 approximately one month in May 2018 (24/04/2018-27/05/2018). Five of the GPS
168 stations were installed directly on the surface of the ice (ARG1-ARG4, ARGG) with four
169 of them integrated with the seismic array (ARG1-ARG4). The remaining two stations
170 (ARG5, ARGR) were placed on solid bedrock next to the glacier near the seismic array.

171 The GPS derived displacement rate (velocity) was computed using a centered moving
172 time window of size ± 3 hrs with a 1 hr time step for east, north, and vertical components,
173 and the combined horizontal components (east + north). This sampling was found to
174 provide the best agreement between errors and signal-to-noise ratio.

175 Seismic observations were continuously recorded at a sample rate of 500 Hz in a grid-like
176 dense array (\varnothing 700 m). The stations were deployed into snow about 30 cm below the
177 surface within the ablation zone of Glacier d’Argentière (see Gimbert et al., 2021, for
178 specific details). Signal preprocessing includes removing the instrument response,
179 detrending and demeaning the continuous waveforms.

180 Temperature and precipitation were monitored at a 10 min sampling rate using one
181 station situated on solid bedrock about a kilometer to the north of the array. Water
182 discharge was measured every 15 min by the Emosson power supply company in
183 excavated tunnels below the glacier tongue (Vincent & Moreau, 2016; Gimbert et al.,
184 2021).

2.2 Matched Field Processing

Matched field processing (MFP) is the natural extension of plane wave beamforming and yields for the location of seismic noise sources in range, depth and azimuth by analysing spherical waves in the close environment of the underlying seismic array (Bucker, 1976). The approach was originally developed in ocean acoustics (Baggeroer et al., 1993; Kuperman & Turek, 1997), but a broad spectrum of applications can be found in environmental seismology to study near-surface processes on the exploration scale (Vandemeulebrouck et al., 2010; Cros et al., 2011; Corciulo et al., 2012; Umlauf & Korn, 2019) and the rapidly emerging special research field of cryoseismology to better understand dynamics within e.g., Alpine glacial ice (Walter et al., 2015, 2020; Umlauf et al., 2021; Nanni et al., 2021, 2022).

Assuming the spatial coherence of the wave field across the array, a systematic correlation of portions of continuous seismic field records and the model-based Green's function (replica) is performed at various candidate source positions. The approach is performed in the frequency domain and can be considered as an equivalent of shift-and-stack techniques in the time domain. For a certain frequency, replica parameterization allows improved data fitting by velocity inversion (Gradon et al., 2019) or polarity optimization for the location of double-couple sources (Umlauf et al., 2021). The procedure is aimed to estimate phase matches between the data wave field and the replica field with the beampower maximum representing the most probable source location.

2.3 Data Features

Data features are statistics of the continuous seismic records from a five-node subarray with high signal-to-noise-ratio, meteorological and water discharge measurements, and events spatially binned from a beamforming catalogue (see Fig. 2 for station locations and a snapshot of the beamforming catalogue). Statistical features were computed for the continuous seismic record of five selected stations shown as inverted white triangles in Fig. 2. We made four copies of the records using a bandpass filter between 10-50 Hz: 10-20 Hz, 20-30 Hz, 30-40 Hz, and 40-50 Hz to cover the frequency bands related to the most dominant processes in glacial ice, such as water flow, crevassing, icequakes or stick-slip tremors (Podolskiy & Walter, 2016). A moving time window of 1 hr is applied to compute the variance, kurtosis, mean, root mean square, skewness, range and

216 interquantile ranges (0.025, 0.25, 0.5, 0.75, 0.95) using ± 3 hrs before and after the
 217 respective time stamp. This sampling matches the GPS data sampling resolution. Hence,
 218 statistical features at every hour reflect the distribution of the seismic data within the
 219 same 6-hours-windows as the averaged GPS data. The meteorological data (temperature
 220 and precipitation) and water discharge measurements are applied by computing the
 221 average of 30 data points (meteorological data) / 24 data points (water discharge
 222 measurements) corresponding to 6 hrs of seismic data (1 data point is the average of the
 223 data during the previous 10 min / 15 min) to obtain consistent feature time windows.

224 We extracted information from an extensive beamforming catalog which was developed
 225 using an advanced matched field processing localization scheme based on a
 226 gradient-descent optimization that meets the challenging, seismically “loud” environment.
 227 A complete detailed description on the methodology and the MFP implementation can be
 228 found in (Nanni et al., 2022). We used four sub-catalogues with center frequencies of 5
 229 Hz, 10 Hz, 15 Hz and 20 Hz. Each catalogue was limited in x,y,z with respect to the
 230 dimension of the array and the depth of the glacier. The seismic velocities were limited to
 231 $1300\text{-}3800 \frac{m}{s}$ and we expect that range to cover Rayleigh wave, P- and S-wave velocities
 232 within glacial ice (Podolskiy & Walter, 2016). We additionally reduced each catalogue to
 233 normalized beampower values between 0.2-1.0. Fig. 2 shows a 1 hr snapshot of a 10
 234 Hz-catalogue together with the ice surface and the bedrock topography. To use the
 235 high-resolution catalogue results as features in the gradient tree boosting model, we
 236 spatially binned the MFP derived sources within 8 predefined source regions of the same
 237 ice volume (voxels V1-V8). Voxels 1-4 capture the deeper part of the glacier, close to its
 238 base, and voxels 5-8 capture the surface equivalent. For each voxel we sum the number of
 239 sources and sum their beampower respectively. For consistency with the other data, we
 240 apply a moving time window of 1 hr using ± 3 hrs before and after the respective time
 241 stamp to match previous feature and label sampling. Virtual cut surfaces and voxel
 242 notations are indicated in Fig. 2.

243 **2.4 Xtreme Gradient Boosting Model for Glacier d’Argentière**

244 Gradient tree boosting (Friedman et al., 2000) is a widely used and scalable supervised
 245 machine learning approach. It is a very powerful tool that is based on, but usually
 246 outperforms, decision tree ensembles (Breiman, 2001; Chen & Guestrin, 2016). Decision
 247 tree ensembles use multiple shallow trees that can be built in a serial manner, in parallel

248 or even independently from each other and combined in a next step in order to enhance
249 model performance. Gradient tree boosting is an extension of decision tree ensembles.
250 The ensemble learner can be used for classification or regression problems. In order to
251 predict a target variable (label), a model is trained based on simple decision rules learned
252 from the data (feature). Depending on the purity of the individual leaves of the tree, the
253 prediction is weighted through a comparison with the respective label. The deviation is
254 represented by an arbitrary loss function. The model is trained sequentially by adding a
255 gradient term to the current decision tree model iteration, with the aim to minimize the
256 loss function for the weighted ensemble of all previous decision trees. Usually, trees that
257 are added in each iteration are shallow (weak learners), but the full ensemble contains a
258 large number of them in total quantity. Once the model is trained, the feature importance
259 (SHAP values) can be evaluated to get more insight into the model drivers allowing one
260 to learn which input observations yield the best estimates on the output label (Lundberg
261 & Lee, 2017).

262 To estimate the GPS velocity on the surface of Glacier d'Argentière, we develop a
263 gradient boosted tree regression model using the features extracted from the data.
264 Specifically, we use the XGBoost package and routines from scikit-learn (Chen &
265 Guestrin, 2016; Pedregosa et al., 2011). When selecting model hyperparameters, the
266 choice of data split, and feature preprocessing is done by iteratively optimizing the model
267 using 5 fold cross validation on the training data to minimize the average
268 mean-squared-error for the folds. A Bayesian optimizer is implemented for a search space
269 to select the best hyperparameters (Head et al., 2018). The procedure randomly selects
270 hyperparameters for 100 iterations, then gradient descent is applied to converge on the
271 best selection for an additional 100 iterations. Initially the search space is large, then
272 expanded or narrowed for specific parameters to avoid final values converging at the upper
273 and lower limits. For each optimization run the evolution of parameters is viewed to
274 update the search space, then the procedure is repeated. The workflow is distributed on a
275 GPU server to train multiple models with different hyperparameters simultaneously to
276 select the final model based on convergence.

277 **2.5 Model development and optimization**

278 To analyze the ability of the model to perform predictions for data with a temporal
279 distance to the training data, we experimented with different train/test splits. First, we

280 experimented with a random train/test split, such that for each test sample, training
 281 samples in close temporal proximity are available. We subsequently increased the length
 282 of consecutive train/test intervals from 24 to 96 hours. For longer intervals, the model
 283 needs to learn time-invariant, globally valid features to still be able to achieve good
 284 performance. As extreme cases, we experimented with 50%/50% splits (where the first
 285 half of the time series is used for training, and the other half is used as test data) and
 286 80%/20% splits (where the first 80% of the time series is used for training and the last
 287 20% for testing). Feature preprocessing included standard scaling (S), quantile
 288 transformation (Q) ($n_quantiles = 50$), principal component analysis (P)
 289 ($n_components = 50$, $whiten = True$), and a random forest regressor (R)
 290 ($n_estimators = 200$, $max_depth = 3$, $n_features_to_select = 20$, $step = 1$). All routines
 291 are available in the scikit-learn package (Pedregosa et al., 2011; Buitinck et al., 2013). We
 292 optimized the hyperparameters for each type of split on the training fraction using the
 293 original data and each possible combination of S, Q, P and R. The results show that the
 294 best-fit model hyperparameters with the lowest loss, hence, the best model, strongly
 295 depends on the choice and combination of data split and feature preprocessing. For each
 296 GPS velocity time series we evaluate the type of split with the choice of preprocessing and
 297 accordingly apply the respective model hyperparameters which yield the highest possible
 298 prediction score. Comparison of data and best-fit model are expressed through the
 299 coefficient of determination (R^2), the root-mean-squared-error ($RMSE$), and the
 300 correlation coefficient (CC). These metrics are applied to allow direct comparison
 301 between models and do not reflect the absolute quality of the results. To further improve
 302 predictions, we tested different applications of a low-pass filter to the GPS velocity time
 303 series to reduce the high-frequency ‘spiky’ fluctuations inherent to the time series. The
 304 cutoff frequency was optimized to maximize the evaluation score.

305 **3 Results**

306 Results are presented to show the capability of the model to predict the velocity time
 307 series for all available RESOLVE GPS stations and specifically highlight the model
 308 predictions for three GPS stations that yield the highest scores (ARG2, ARG3 and ARGG
 309 in Fig. 1). Additionally, we provide details on the best-fit model hyperparameters for
 310 station ARG3 considering the implementation of different data splits and feature
 311 preprocessing.

312 We assess the different types of data splitting for model evaluation and provide results for
 313 a direct comparison of the performance and robustness of each technique. In Fig. 3 we
 314 show the prediction scores for CC and $RMSE$ using the testing fraction of the GPS
 315 velocity time series of ARG3 for different short-term and long-term splits, and the
 316 dependence on feature smoothing window length between 1-24 hrs to reduce bias from
 317 temporary signals. The results indicate the model performance is strongly dependent on
 318 the type of data split and that it generally improves when larger smoothing windows are
 319 applied. The best results are observed when using random splits, where the entire time
 320 series is shuffled before selecting the training and test data, with a $CC > 0.8$ for a
 321 smoothing window >5 hrs. Increasing the smoothing window length further improves the
 322 predictions towards $CC = 1$ (Fig. 3 [a]). Similar metrics are observed with the
 323 $RMSE < 1$ using a window length >7 hrs and further decreasing to $RMSE = 0.25$ with
 324 longer windows (Fig. 3 [b]). These results show the best model fit but this split does not
 325 encourage the model to learn time-invariant features, as no predictions for data with large
 326 temporal distance to the training data have to be made.

327 To maintain temporal sequencing, we split the data into uniform temporal blocks with
 328 sizes between 24-96 hrs for the entire duration of the data. The best results are found
 329 using temporal block sizes of 24 and 36 hrs with $CC > 0.6$ ($RMSE < 1.2$) for a window
 330 length >9 hrs. The results improve to $CC = 0.8$ ($RMSE = 0.75$) for the largest
 331 smoothing windows tested and increase with an approximate linear trend (Fig. 3).
 332 Applying block sizes >36 hrs show inconsistent, alternating behavior with little
 333 improvement above $CC = 0.6$ ($RMSE < 0.6$). This is consistent when using even larger
 334 fractions of the data for the long-term splits (80%/20% split, 50%/50% split). In general,
 335 these models show a $CC < 0.2$ ($RMSE > 0.65$) with the maxima derived using a
 336 smoothing window between 9-13 hrs.

337 The sensitivity of the best-fit model hyperparameters applying different data splits and
 338 feature preprocessing is illustrated in Fig. 4. Variations in the hyperparameters are
 339 strongly dependent on and significantly differ for the type of split and the choice of
 340 feature preprocessing. Except for $n_estimators$ ranging between about 1000-1200 for all
 341 types of split, no trend can be observed for other hyperparameters and types of split (4
 342 [a]). Just as the data split alters the model, different choices and combinations of feature
 343 preprocessing lead to inconsistent model hyperparameters. Values of min_child_weight
 344 seem to be lower when less preprocessing is applied, but overall the response of the model

345 hyperparameters shows no clear pattern for different choices of preprocessing. Comparing
 346 the models of three equally 50%/50% split GPS stations (ARG2, ARG3, ARGG) in terms
 347 of hyperparameters, preprocessing, and low-pass filtering indicates the requirements for
 348 the best prediction score ($CC = 0.25 - 0.46$) are also fundamentally different and
 349 significantly influence the model performance (Fig. 1).

350 **3.1 Short-term sliding predictions**

351 The model predictions for the velocity time series of GPS station ARG3 using three
 352 different types of train/test split are shown in Fig. 5. For the testing set, data versus
 353 model correlations are shown in the inset. Without any additional preprocessing applied
 354 to the features except smoothing to suppress noise (smoothing window of 15 hrs), the
 355 random split yields outstanding performance (Fig. 5 [a]) with $RMSE = 0.42$, $CC = 0.94$,
 356 and $R^2 = 0.88$. The model is able to capture hourly fluctuations by randomly training
 357 and testing on the time sampling domain of the data (1 hr).

358 Next, we increase the length of train/test intervals in the range of 24 and 96 hours. The
 359 most robust and performant model with a reasonable agreement between smoothing and
 360 prediction score was achieved using blocks of 36 hrs and smoothed features with a
 361 smoothing window of 15 hrs (Fig. 5 [b]). Compared to using blocks of 24 hrs, the 36 hrs
 362 block split model shows slight deficiencies expressed by a lower RMSE in the range of
 363 about 0.2, which is not reflected by the CC. This marginal shortcoming is
 364 counterbalanced by the gain in block size from 24 hrs to 36 hrs, leading to a gain in
 365 prediction horizon of 12 hrs which serves the scientific motivation of this study. Without
 366 any additional feature preprocessing applied, the model scores with $RMSE = 0.84$,
 367 $CC = 0.75$ and $R^2 = 0.5$ (Fig. 5 [b]). Apart from some infrequent failures and not fully
 368 capturing the amplitude at all times, the model is able to predict fluctuations with daily
 369 resolution.

370 **3.2 Long-term sliding predictions**

371 With the aim to stretch the prediction horizon, we apply a 50%/50% split, since the
 372 model seems to be less sensitive towards smoothing than the one using the 80%/20% split
 373 we consider it more robust (Fig. 3). We train the model on the first half of the data and
 374 test it on the remaining half. Analogous to the short-term splits, we use the raw features

375 and only apply a smoothing window length of 15 hrs in a first iteration, which results in a
 376 significantly lower prediction score ($CC < 0.4$, $RMSE > 0.9$, see also Fig. 3). Extensive
 377 feature preprocessing involving S, Q, P and R, and the additional application of a
 378 low-pass filter with a cutoff frequency of 16.5 hrs improves the correlation coefficient up to
 379 $CC = 0.47$ (Fig. 5 [c]). While short-term dynamics can not be captured by the model, it
 380 is able to predict the long-term behavior of the GPS velocity, notable the varying trend
 381 but with a static offset.

382 **3.3 Sliding predictions across Glacier d’Argentière**

383 Next we evaluate short-term model predictions (block split, 36 hrs) and long-term model
 384 predictions (50%/50% split) for three GPS stations (ARG2, ARG3 and ARGG in Fig. 1),
 385 which yield the highest prediction scores within the network. We do not apply any feature
 386 preprocessing except a smoothing window of 15 hrs, unlike the feature preprocessing (S,
 387 Q, P, R) and an additional lowpass filter for long-term predictions to enhance the model
 388 performance.

389 For GPS station ARG2, which was located within the seismic array and situated close to
 390 seismic node 64 (Fig. 2), we derive a model score of $CC = 0.25$ using a 50%/50% split
 391 with preprocessing P and a low-pass filter with a cutoff frequency of 2.5 hrs applied (see
 392 Table 1 for best-fit model hyperparameters). The SHAP features show that statistical
 393 features of node 12 contributed most to the model (Fig. A2 [a]). It is important to note
 394 that node 12 was situated on the north-western flank of the glacier while ARG2 was
 395 located in the central-north close to the glacier tongue. The interstation distance and the
 396 model’s decision “against” favoring features from the closest node 64 posit that the
 397 long-term behavior of the surface velocity of the ice is likely not locally driven by e.g., an
 398 opening crevasse, but rather controlled by some seismic activity along the north-western
 399 flank. As displayed in Fig. 6 [a] short-term predictions (36 hrs blocks, smoothing window
 400 of 15 hrs) for ARG2 yield an increase in CC by a factor of 2.64. The SHAP features
 401 (Fig. 7 [a]) show that beamforming features replace statistical features when analyzing
 402 shorter time windows. Explicitly, the low-frequency source locations (5 Hz) within lower
 403 voxel V1 (Fig. 2) contributed most to the model predictions followed by the skewness of
 404 seismic node 12 in the 30-40 Hz filter band.

405 GPS station ARG3 was situated in line with ARG2 and integrated with the seismic array
 406 as well. More precisely it is located next to seismic node 60. For long-term predictions
 407 (50%/50% split), we derive a model score of $CC = 0.46$ with preprocessing S, Q, P and R
 408 and a low-pass filter with a cutoff frequency of 16.5 hrs applied (see Table 1 for best-fit
 409 model hyperparameters). When comparing to ARG2, more preprocessing and a stronger
 410 filter are applied. As a result of the smoother GPS data from the low-pass filter data, the
 411 model shows a CC value with a 2x increase. As revealed by the SHAP features and as for
 412 ARG2, statistics from node 12, situated at the north-western flank of the glacier, are of
 413 upmost importance (Fig. A2 [b]). Fig. 6 [b] shows the equivalent short-term predictions
 414 (36 hrs blocks, smoothing window of 15 hrs) for ARG3 which result in $CC = 0.75$. Again,
 415 statistical features important for long-term predictions are here replaced by low-frequency
 416 beamforming features (5 Hz) from the lower voxels V1 and V2 (Fig. 7 [b], Fig. 2).
 417 Additionally, the 0.5 interquartile range of the 30-40 Hz filtered record of seismic node 80
 418 strongly contributes to the model predictions.

419 For GPS station ARGG situated within the accumulation zone of the glacier <3 km
 420 north-west from the seismic array, the best long-term model score based on a 50%/50%
 421 split is $CC = 0.37$ with a low-pass filter with a cutoff frequency of 1.39 hrs applied (see
 422 Table 1 for best-fit model hyperparameters). The data features were best suited in the
 423 original format (no preprocessing) using the filter to suppress short-term dynamics. As for
 424 ARG2 and ARG3, the SHAP features again indicate the importance of statistical features
 425 from seismic node 12 (Fig. A2 [c]). For short-term predictions (36 hrs block split) we
 426 derive a $CC = 0.6$, which is mostly dependent on beamforming features of the lower voxel
 427 V2 (Fig. 2) in the 20-30 Hz filter band followed by the 0.5 interquartile range of the 40-50
 428 Hz filtered record of seismic node 64 and the skewness of the 40-50 Hz filtered record of
 429 seismic node 12.

430 The long-term model results and the related feature ranks for the three GPS stations
 431 analyzed show consistent results that suggest glacial surface velocity is being controlled by
 432 activity at the north-western flank of the glacier. Interestingly, the meteorological features
 433 and surface beamforming voxels generally play a subordinate role for the model estimates.
 434 For short-term model predictions we observe that beamforming features of the lower
 435 voxels close to the glacier bed are most important followed by high-frequency statistical
 436 features (30-50 Hz), such as the 0.5 interquartile range and the skewness.

4 Discussion

The application of machine learning using continuous seismic records continues to show success in describing physical processes of complex natural systems. While the glacier motion model predictions are not as robust as those for laboratory stick-slip studies (Rouet-LeDuc, Hulbert, Bolton, et al., 2018; Shokouhi et al., 2021; Corbi et al., 2019; Jaspersen et al., 2021; Wang et al., 2021), slow slip in Earth (Hulbert et al., 2020), future prediction (Laurenti et al., 2022; Wang et al., 2022), or stick-slip processes in Earth (Johnson & Johnson, 2021), they are nonetheless predictive for the log-term sliding behavior and especially performant for short-term variations. Ice deformation is considered mostly aseismic through viscous creep (Gimbert et al., 2021), which is inherent to the material properties. The data features are designed to capture such deformation using information in the continuous signal emitted from internally deforming slip boundaries during viscous flow, which occurs at a range of pressures and temperatures. The glacial system dynamics are highly complex and variations in signals produced by the sources of noise appear to be more heterogeneous than in a laboratory system or an earthquake fault.

This study shows for the first time that surface displacement rates can be linked to distinct areas, and even in-depth activity, of a temperate Alpine glacier based on the seismic beamforming features. The addition of seismic beamforming as a data feature provides additional information to the model space and enables the estimate of surface displacement rates on Alpine glacial ice in an highly dynamic and noise-prone environment, and the ability to locate its driving process. To our current state of knowledge, basal motion is most likely the driver for deep cryoseismogenic processes which drive the displacement rates at the surface of Glacier d'Argentière and outwards internal deformation through viscous creep due to its strong seismic fingerprint (Podolskiy & Walter, 2016).

Data splits strongly influence the decision tree models outcome with sample-wise or short-term train/test fractions leading to the highest prediction scores and longer train/test fractions to a subsequent decrease in performance together with a loss in robustness. Even though the short-term models outperform the long-term models in terms of evaluation metrics, they provide less insights into the physics and dynamics of glacial sliding. Hence, there is a tradeoff between model performance and long-term predictions.

469 We found that the best agreement between prediction horizon and model performance is
470 given by using block splits with block sizes of 24-36 hrs ($CC = 0.75$). Those models are
471 robust towards feature smoothing, meaning that within each block the dynamics and
472 processes are similar and hence ‘understandable’ for the model.

473 The best long-term model captures the long wavelength characteristics, suggesting that
474 the highly variable temporal fluctuations are generated by a number of incoherent
475 processes and the model can not isolate into these unique characteristics in the feature
476 space. A possible cause is the seismic features contain a combination of information from
477 multiple weak processes and expanding the feature space might improve the high
478 frequency estimates. With the current best model and features, the surface ice velocity
479 can be predicted with an accuracy of up to 46% for the longer term behavior in the range
480 of 16.5 hrs.

481 Intensively studying the hyperparameter space and the dependence on data split, different
482 choices of preprocessing and low-pass filters shows that each station-related model has to
483 be tuned independently and model settings may not be generalized in the Alpine
484 cryospheric environment. We found that individual station estimates generally score
485 better than averages of multiple on-ice velocity time series and that bedrock stations were
486 less suited for the analysis.

487 Overall, we observe that the relevant features for model predictions differ for GPS stations
488 that were situated in the noise-prone ablation zone (ARG2, ARG3) compared to ARGG,
489 which was situated in the accumulation zone. For ARGG, less influenced by cryoseismic
490 sources as e.g. crevassing or water flow, which can potentially mask in-depth activity of
491 the glacier, the long-term model and short-term model can both pick up processes at the
492 glacier’s base relevant for sliding (lower beamforming voxels V2 and V4, 20-30 Hz). For
493 long-term model predictions of ARG2 and ARG3 those features are revised by statistical
494 features, as they potentially reflect the dominant local sources such as crevassing or water
495 flow. The short-term models of ARG2 and ARG3 however capture in-depth activity. We
496 observe consistent results for both stations in favoring low-frequency beamforming
497 features from the bottom voxels V1 and V2 (5 Hz).

498 The RESOLVE experiment design was most advantageous for capturing the
499 spatio-temporal seismic and geodetic behavior driven by glacial processes in the one
500 month of data collection. Limitations to the seismic and geodetic measurements as

501 applied to this analysis include the discrepancy in sampling rate (500 Hz for seismic
502 observations vs. 1 hr for geodetic observations). This mismatch requires several steps of
503 preprocessing to properly align the data features and labels, specifically the moving time
504 window analysis and smoothing of the time series data or the compilation of the highly
505 resolved beamforming catalogue. Those procedures come with a potential loss of
506 information regarding short-term variations of the glacier's activity. Furthermore, seismic
507 observations were solely collected in the ablation zone of the glacier, while GPS station
508 coverage spanned over the entire length of Glacier d'Argentière (<3 km). The
509 accumulation zone of temperate based glacial ice is typically less active than the ablation
510 zone. The ablation zone, however, is characterized by a multitude of physical processes
511 such as crevasse formation, meltwater flow or avalanches and rockfalls provoked by
512 increasing temperatures in lower altitudes (Nanni et al., 2022). Even though the geodetic
513 observations show coherent behavior across the network and the glacier's extent (Fig. A1),
514 model predictions of distant stations which were situated in the accumulation zone may
515 be challenged due to regime differences. Compared to predictions made on GPS stations
516 which were integrated with the seismic array, model estimates of high-altitude geodetic
517 observations show reasonable performance, but might have benefited from nearby seismic
518 observations.

519 The mild power threshold of the beamforming catalogue (0.2-1.0) subsequently leads to
520 the integration of poorly resolved seismic sources in our analysis which poses the risk to
521 decrease the model performance due to random, physically unconstrained locations.
522 However, in view of the high noise level in Alpine glacial environments, locations with a
523 lower resolution likely carry relevant information from deep processes at the glacier bed,
524 as e.g. basal stick-slip (Umlauf et al., 2021) or subglacial water flow (Nanni et al., 2020).
525 As revealed by the feature importance for model estimates of GPS ARGG (Fig. 7 [c]) the
526 20 Hz beamforming catalogue as applied to this analysis carries information enabling the
527 best model prediction. The surface displacement itself but also the center frequency of the
528 catalogue reasons that glacier basal motion, potentially coupled with subglacial water
529 flow, is most likely the driving mechanism for the displacement of ARGG, as pure
530 subglacial water flow is characterized by lower frequencies (3-7 Hz) (Nanni et al., 2020)
531 and does not ultimately lead to surface displacement.

532 We have learned that this line of analysis could potentially contribute to an improvement
533 of glacial sliding laws by considering relevant drivers for model parameterizations that are
534 revealed by the feature importance.

535 **5 Conclusions**

536 A profound understanding and the formulation of sliding laws for glacier basal motion are
537 still a major challenge for the scientific community and needed for hazard assessment and
538 the generation of new prediction models. Especially for temperate glaciers in Alpine
539 regions, sliding is difficult to monitor with conventional geophysical approaches. On-ice
540 seismological records prove to be a very rich archive of glacial activity, but due to glacial
541 noise from other cryoseismic sources, stick-slip events and tremors are often masked and
542 remain unnoticed. New approaches are needed which involve on-ice seismological
543 measurements densely sampled in space and time, as well as modern tools that efficiently
544 analyze such large datasets and reveal previously hidden signals.

545 We applied a supervised ML approach gradient tree boosting to a seismic array data set
546 acquired in course of the RESOLVE project on Glacier d'Argentière and showed its
547 general suitability for the identification of seismic signatures of ice beds in the presence of
548 melt-induced microseismic noise. The analysis is designed to verify if model estimates are
549 driven by basal motion. Our results demonstrate that gradient tree boosting is a suitable
550 tool to estimate ice surface displacement rates from seismic data collected at glaciers and
551 that information about basal processes can be accessed from on-ice seismometers,
552 analogous to frictional behavior of tectonic fault zones, at least at long period. We have
553 learned that other than for quiet laboratory faults (Rouet-LeDuc, Hulbert, Bolton, et al.,
554 2018) or reasonably long monitoring time series along tectonic faults (Rouet-LeDuc,
555 Hulbert, & Johnson, 2018; Johnson & Johnson, 2021), using only statistical properties of
556 continuous seismic records are not sufficient to describe glacial environments. We adapted
557 the ML model by creating expressive beamforming features using array processing that
558 meet the challenging, seismically “loud” environment. As revealed by the feature
559 importance, the spatio-temporal compilation of seismic source locations provides the
560 essential information for the model to relate estimates of surface velocities to in-depth
561 activity.

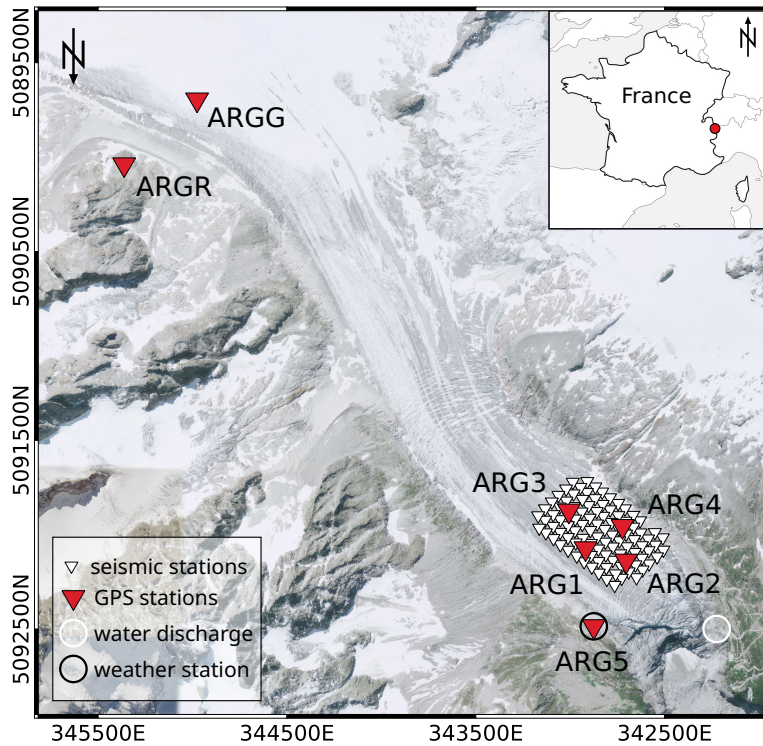


Figure 1. Overview map of Glacier d'Argentière together with the RESOLVE sensor infrastructure (Gimbert et al., 2021) including the locations of the seismic nodes (white triangles), the GPS stations (red triangles, ARGx), the weather station (black circle around ARG5) and the location of the borehole for measurements of water discharge (white circle). The GPS stations ARG1, ARG2, ARG3, ARG4 and ARGG were installed on the surface of the glacier (on-ice stations), GPS stations ARG5 and ARGR were installed on solid ground / bedrock (off-ice stations).

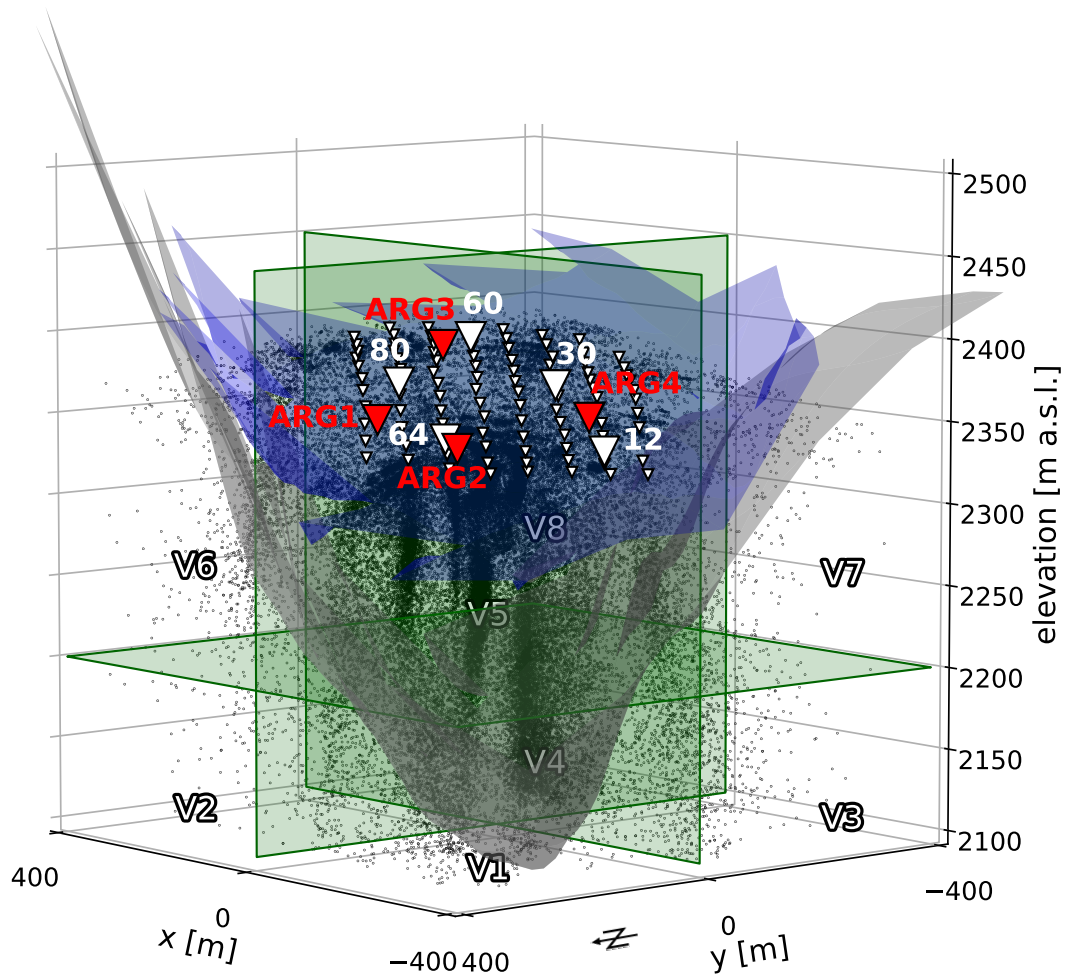


Figure 2. Snapshot of the thresholded beamforming catalogue together with the drone derived ice surface (shades of blue) and the bedrock topography measured by radio-echo sounding (shades of grey). Black dots represent seismic source locations during 1 hr (temporal resolution of 1 sec), for a center frequency of 10 Hz and beampower values between 0.2-1.0. The white triangles indicate the seismic array with the five heightened ones being the selected stations for the computation of the statistical features (12, 30, 60, 64, 80). The red triangles display GPS stations (ARG1-ARG4) situated within the seismic array. The green planes indicate the cut surfaces that divide the glacier into eight voxels (V1-V8) with V1-V4 capturing the lower part close to the glacier bed and V5-V8 encompassing portions of the ice surface.

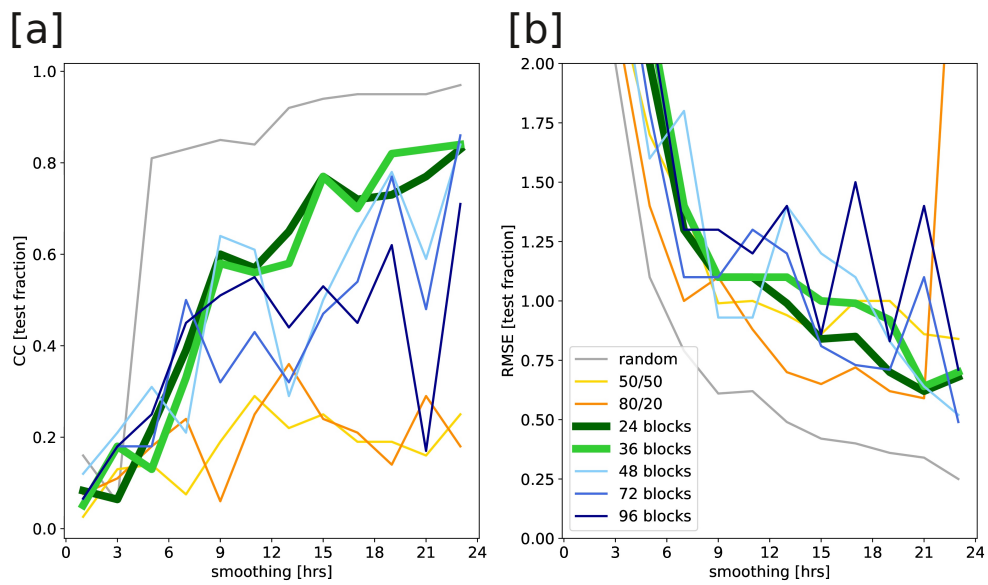


Figure 3. Model prediction scores ([a] *CC* and [b] *RMSE*) of the testing velocity time series of GPS station ARG3 in dependence on the degree of smoothing window duration applied to the features. Blocks refer to the lengths of the train/test intervals. No additional feature preprocessing was applied.

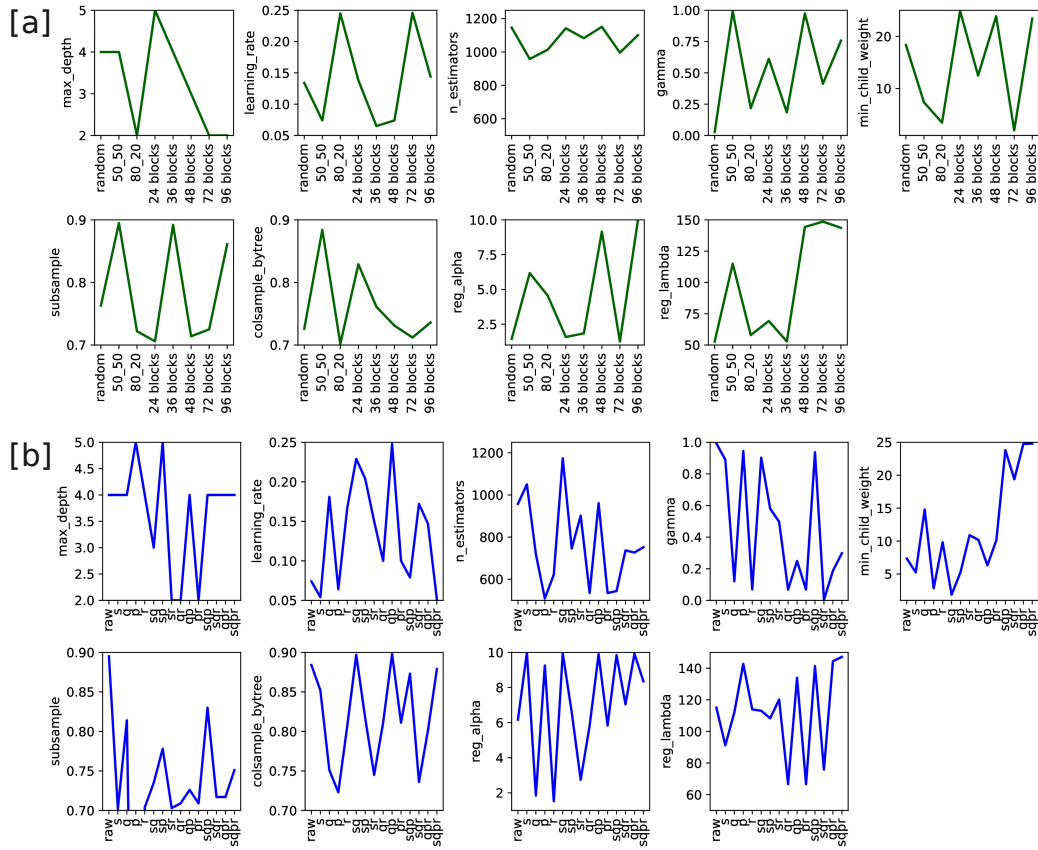


Figure 4. [a] Best-fit model hyperparameters optimized for different types of data split applied to the model of GPS station ARG3. The data was used in the original format with no additional preprocessing applied. [b] Best-fit model hyperparameters optimized for the raw data and all available combinations of preprocessing. Data were split 50%/50%.

Table 1. Overview of best-fit model hyperparameters, choices of preprocessing and low-pass filters applied to GPS stations ARG2, ARG3, ARGG using a 50%/50% split.

		GPS stations		
		ARG2	ARG3	ARGG
Hyperparameters	max_depth	5	4	3
	learning_rate	0.052	0.051	0.052
	n_estimators	514	752	527
	gamma	0.816	0.298	0.696
	min_child_weight	1.28	24.803	23.946
	subsample	0.708	0.751	0.738
	colsample	0.771	0.879	0.732
	reg_alpha	9.849	8.349	1.929
	reg_lambda	100.271	147.171	134.623
Preprocessing		P	S,Q,P,R	-
Low-pass filter [hrs]		2.5	16.5	1.39
Correlation coefficient		0.25	0.46	0.37

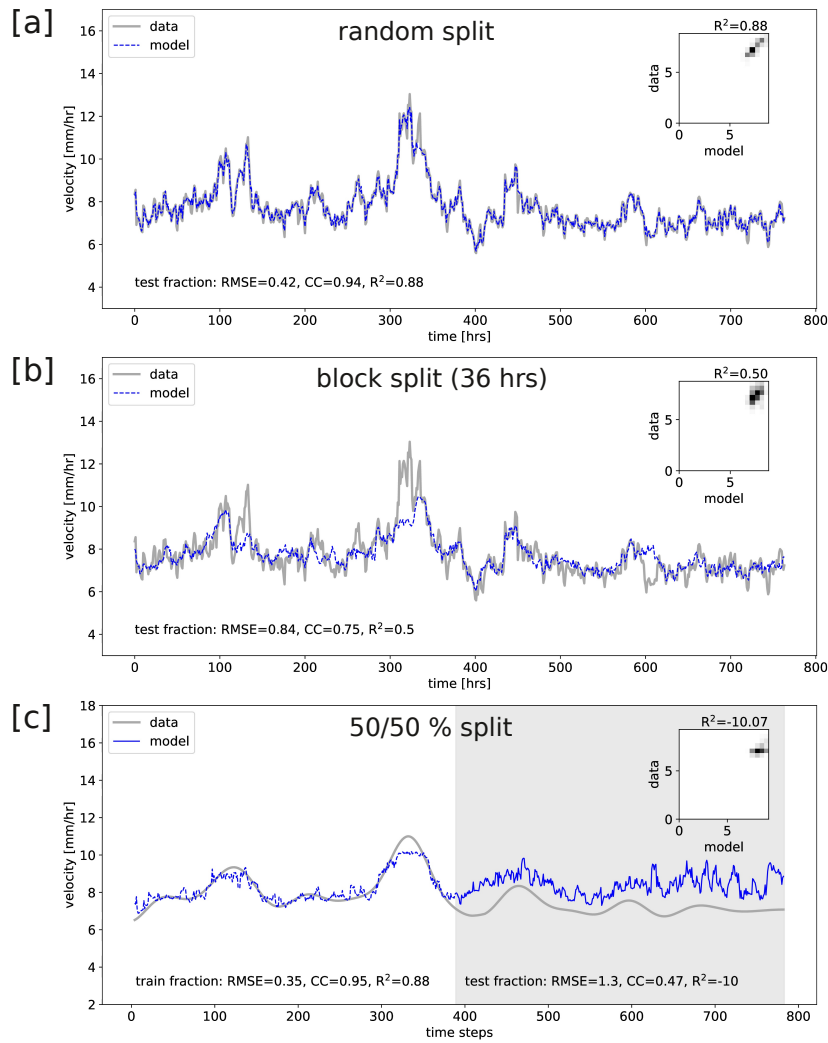


Figure 5. Performance of the XGB model to predict surface velocity [mm/hrs] trained on GPS station ARG3 (see Fig. 1 and Fig. 2), which was situated within the seismic array in the ablation zone of Glacier d'Argentière. The model performance is compared for different types of split applying the respective best-fit model hyperparameters. The data curve is displayed in grey and the model predictions in blue. [a] The model was trained and tested on random samples. No additional preprocessing was applied. [b] The model was trained and tested using blocks of 36 hrs. No additional preprocessing was applied. [c] The model was trained on 50 % of the velocity time series (white facecolor) and tested on the remaining 50 % (grey facecolor). Preprocessing involved S,Q,P,R and a low-pass filter with a cutoff frequency = 16.5 hrs was applied.

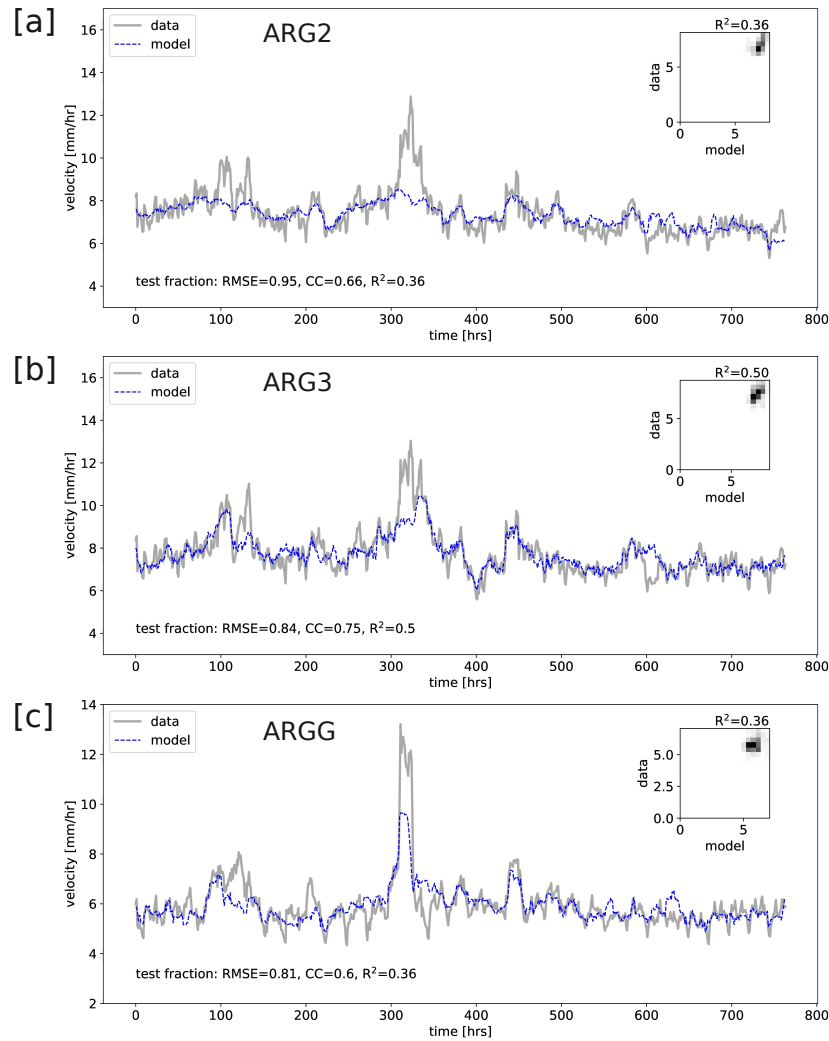


Figure 6. Performance of the XGB model to predict surface velocity [mm/hrs] using blocks of 36 hrs for training and subsequent testing. The model was trained and tested on GPS station ARG2 [a], ARG3 [c] and ARGG [e] (see Fig. 1 and Fig. 2). The feature importance is expressed through SHAP values to the right of the predictions respectively ([b], [d], [e]). The best-fit model hyperparameters were optimized for all three models and data were smoothed over 15 hrs. No additional preprocessing was applied.

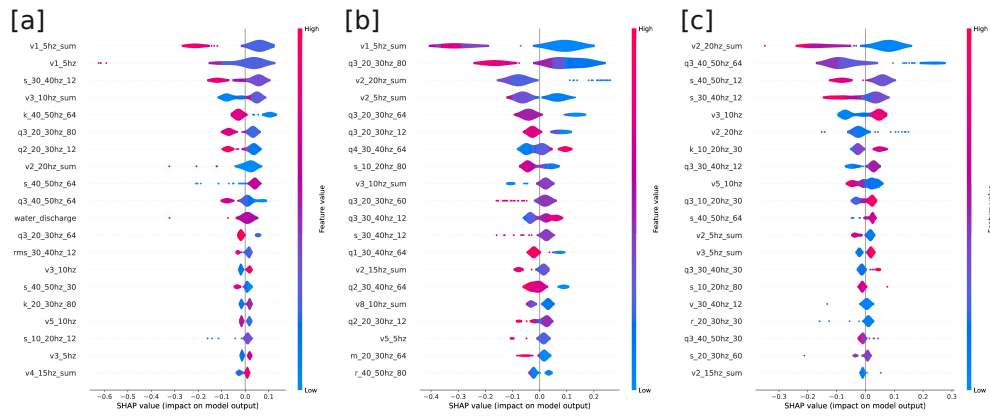


Figure 7. Feature importance (SHAP values) for model predictions using block sampling (block size = 36 hrs) shown in Fig. 6: [a] ARG2, [b] ARG3, [c] ARGG.

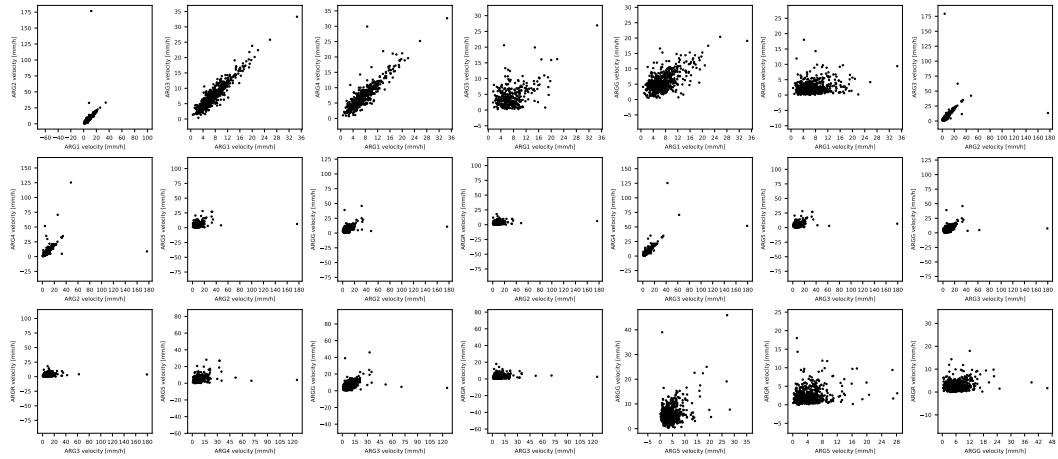


Figure A1. Station-wise correlation of geodetic observations.

562 Appendix A

563 The RESOLVE GPS (GNSS) analysis has been performed by a static, differential
 564 positioning using the GAMIT software (Herring et al., 2018) in a network combining the 5
 565 RESOLVE GNSS stations (ARG1-4 on the glacier and ARG5 beside the glacier on the
 566 bedrock), plus the ISTERre long-term station ARGG on Glacier d'Argentière outside the
 567 RESOLVE network, with 14 permanent and stable RENAG (<http://renag.resif.fr>) stations
 568 in less than 180 km distance (including ARGG on bedrock close to Glacier d'Argentière at
 569 3 km distance from the RESOLVE network). This set of stations has been analyzed in
 570 6-hours-sessions (corresponding to 30-40 mm of displacement of stations on Glacier
 571 d'Argentière) shifted by 1 hour to obtain hourly positions for each of the stations. The
 572 formal uncertainties of each of the position estimates are 2-3 mm on the horizontal
 573 components. The positioning of the bedrock site ARG5, close to the glacier stations and
 574 therefore in a comparable environment, indicates a dispersion of 4-6 mm. This value is
 575 probably a realistic estimate of the hourly positioning precision of the glacier stations.

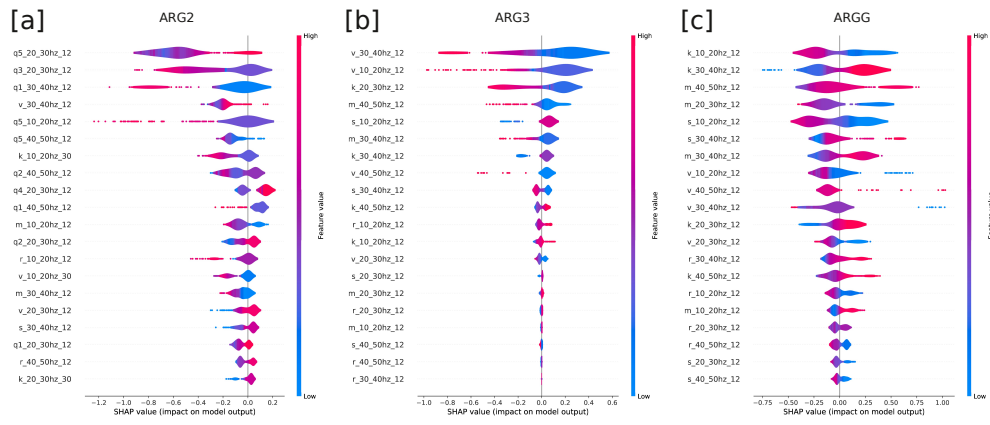


Figure A2. Feature importance (SHAP values) for model predictions using a 50%/50% split on the velocity time series of [a] ARG2, [b] ARG3, [c] ARGG.

576 **Acknowledgments**

577 The authors acknowledge the financial support by the Federal Ministry of Education and
578 Research of Germany and by the Sächsische Staatsministerium für Wissenschaft Kultur
579 und Tourismus in the program Center of Excellence for AI-research "Center for Scalable
580 Data Analytics and Artificial Intelligence Dresden/Leipzig", project identification number:
581 ScaDS.AI CWJ and PAJ acknowledge support by the U.S. Department of Energy, Office
582 of Science, Office of Basic Energy Sciences, Chemical Sciences, Geosciences, and
583 Biosciences Division under grant 89233218CNA000001. CWJ also acknowledges
584 Institutional Support (Laboratory Directed Research and Development) at Los Alamos
585 National Laboratory. This work has been conducted in the framework of the RESOLVE
586 Project (<https://resolve.osug.fr/>; LabEx OSUG@2020, Investissement d'avenir –
587 ANR10LABX56 and IDEX Université Grenoble Alpes). The seismic nodes and GPS
588 stations were provided and operated by the French seismological and geodetic network
589 Résif-Epos. The computations of the beamforming catalogue were performed using the
590 GRICAD infrastructure (<https://gricad.univ-gre-noble-alpes.fr>), which is supported by
591 Grenoble research communities, and with the CiGri tool
592 (<https://github.com/oar-team/cigri>) that was developed by Gricad, Grid5000
593 (<https://www.grid5000.fr>) and LIG (<https://www.liglab.fr/>). The machine Learning
594 model was developed using the resources of the Leipzig University Computing Centre.

595 **Open Research Section**

596 **Data Availability**

597 The MFP source codes are described and available via
598 <https://lecoinal.gricad-pages.univ-grenoble-alpes.fr/resolve/> (last access: 11/11/2021)
599 under a creative commons attribution 4.0 international license. The data derived from
600 the MFP analysis (i.e., 29 sources localizations per second over 34 days and for 20
601 frequency bands) together with 1 day of raw seismic signal recorded over the 98 seismic
602 stations are available via <https://doi.org/10.5281/zenodo.5645545> under a creative
603 commons attribution 4.0 international license (Nanni, Roux, et al., 2021). The complete
604 set of raw seismic data can be found at <https://doi.org/10.15778/resif.zo2018> under a
605 creative commons attribution 4.0 international license. The GPS data are available on
606 request through Andrea Walpersdorf (andrea.walpersdorf@univ-grenoble-alpes.fr).

Credit Author Statement

J.U. and C.W.J. formulated most of the manuscript, computed the data features and performed the machine learning analysis including hyperparameter optimization. All steps were supported by P.A.J. throughout the project. P.R. and A.L. performed MFP and compiled the beamforming catalogue. A.W. processed the GPS data. U.N. and F.G. supported the study with discussions on characteristics of Alpine glaciers. S.L and S.M. implemented data split techniques. Together with D.T., B.R.-L., C.H. and P.A. the first authors conceptualized the project and had fruitful discussions on the machine learning analysis.

References

- Aster, R., & Winberry, R. (2017). Glacial Seismology . *Reports on Progress in Physics*, 80.
- Baggeroer, A., Fellow, IEEE, Kuperman, W., & Mikhalevsky, P. (1993). An Overview of Matched Field Methods in Ocean Acoustics. *IEEE Journal of Oceanic Engineering*, 18(4), 401–424.
- Barcheck, C., Tulaczyk, S., Schwartz, S., Walter, J., & Winberry, J. (2019). Implications of basal micro-earthquakes and tremor for ice stream mechanics: Stick-slip basal sliding and till erosion . *Earth and Planet, Sci. Lett.*, 486, 54–60.
- Breiman, L. (2001). Random Forests . *Machine Learning*, 45, 5–32.
- Bucker, H. (1976). Use of calculated sound fields and matched-field detection to locate sound sources in shallow water. *Journal of Acoustical Society of America*, 59(2), 368–373.
- Buitinck, L., Louppe, G., Blondel, M., Pedregosa, F., Mueller, A., Grisel, O., . . . Varoquaux, G. (2013). API design for machine learning software: experiences from the scikit-learn project. In *Ecml pkdd workshop: Languages for data mining and machine learning* (pp. 108–122).
- Chen, T., & Guestrin, C. (2016). XGBoost: A scalable tree boosting system . In *Proceedings of the 22nd ACM SIGKDD International Conference on Knowledge Discovery and Data Mining*. New York: ACM, 785–794.
- Corbi, F., Sandri, L., Bedford, J., Funicello, F., Brizzi, S., Rosenau, M., & Lallemand, S. (2019). Machine learning can predict the timing and size of analog earthquakes. *Geophysical Research Letters*, 46, 1303 - 1311.

- 639 Corciulo, M., Roux, P., Campillo, M., Dubucq, D., & Kuperman, W. (2012). Multiscale
640 matched-field processing for noise-source localization in exploration geophysics.
641 *Geophysics*, *77*(5), KS33–KS41.
- 642 Cros, E., Roux, P., Vandemeulebrouck, J., & Kedar, S. (2011). Locating hydrothermal
643 acoustic sources at Old Faithful Geyser using Matched Field Processing. *Geophysical*
644 *Journal International*, *187*, 385–393.
- 645 Cuffey, K., & Paterson, W. (2010). *The Physics of Glaciers*. Academic Press.
- 646 Dorostkar, O., Guyer, R., Johnson, P., Marone, C., & Carmeliet, J. (2017). On the
647 micromechanics of slip events in sheared, fluid-saturated fault gouge. *Geophysical*
648 *Research Letters*, *44*, 6101–6108.
- 649 Eibl, E., Bean, C., Einarsson, B., Pålsson, F., & Vogfjörð, K. (2020). Seismic ground
650 vibrations give advanced early-warning of subglacial floods. *Nature*
651 *Communications*, *11*(1), 1–11.
- 652 Faillettaz, J., Funk, M., & Vincent, C. (2015). Avalanching glacier instabilities: Review
653 on processes and early warning perspectives. *Rev. Geophys.*, *53*, 203–224.
- 654 Friedman, J., Hastie, T., & Tibshirani, R. (2000). Additive Logistic Regression: A
655 Statistical View of Boosting. *The Annals of Statistics*, *28*(2), 337–407.
- 656 Gagliardini, O., Cohen, D., Råback, P., & Zwinger, T. (2007). Finite-element modeling
657 of subglacial cavities and related friction law. *Journal of Geophysical Research*,
658 *112*, 1–11.
- 659 Gimbert, F., Nanni, U., Roux, P., Helmstetter, A., Garambois, S., Lecointre, A., . . .
660 others (2021). A multi-physics experiment with a temporary dense seismic array on
661 the argentière glacier, french alps: The resolve project. *Seismological Society of*
662 *America*, *92*(2A), 1185–1201.
- 663 Glen, J. (1955). The creep of polycrystalline ice. *Proceeding of the Royal Society of*
664 *London, Series A*, *288*, 519–538.
- 665 Gradon, C., Moreau, L., Roux, P., & Ben-Zion, J. (2019). Analysis of surface and seismic
666 sources in dense array data with match field processing and Markov chain Monte
667 Carlo sampling. *Geophysical Journal International*, *218*, 1044–1056.
- 668 Gräff, D., Knöpfli, M., Lipovsky, B., Selvadurai, P., Farinotti, D., & Walter, F. (2021).
669 Fine structure of microseismic glacial stick-slip. *Geophysical Research Letters*, *48*.
- 670 Head, T., MeachCoder, Louppe, G., Shcherbatyi, I., fcharras, Vinícius, Z., . . . Fabisch, A.
671 (2018). scikit-optimize/scikit-optimize: v0.5.2. *Zenodo*.

- 672 Helanow, C., Iverson, N., Woodard, J., & Zoet, L. (2021). A slip law for hard-bedded
673 glaciers derived from observed bed topography . *Science Advances*, *7*(20), 1—8.
- 674 Helmstetter, A., Nicolas, B., Comon, P., & Gay, M. (2020). Basal icequakes recorded
675 beneath an Alpine glacier (Glacier d'Argentière, Mont Blanc, France): Evidence for
676 stick-slip motion? . *Science*, *368*(6486), 76—78.
- 677 Herring, T., King, R., M.A., F., & McClusky, S. (2018). Gamit reference manual, gps
678 analysis mit, release 10.7. *Department of Earth, Atmospheric and Planetary*
679 *Sciences, Massachusetts Institute of Technology, Cambridge, MA*.
- 680 Hudson, T., Brisbourne, A., Walter, F., Gräff, D., White, R., & Smith, A. (2020).
681 Icequake source mechanisms for studying glacial sliding . *Journal of Geophysical*
682 *Research: Solid Earth*, *125*(11).
- 683 Hulbert, C., Rouet-LeDuc, B., Johnson, P., Ren, C., Riviere, J., Bolton, D., & Marone, C.
684 (2019). Similarity of fast and slow earthquakes illuminated by machine learning .
685 *Nature Geoscience*, *12*, 69–74.
- 686 Hulbert, C., Rouet-Leduc, B., Jolivet, R., & Johnson, P. (2020, 08). An exponential
687 build-up in seismic energy suggests a months-long nucleation of slow slip in cascadia.
688 *Nature Communications*, *11*, 4139. doi: 10.1038/s41467-020-17754-9
- 689 Iken, A. (1981). The effect of the subglacial water pressure on the sliding velocity of a
690 glacier in an idealized numerical model . *Journal of Glaciology*, *27*(97), 407—421.
- 691 Jaspersen, H., Bolton, D., Johnson, P., Guyer, R., Marone, C., & de Hoop, M. (2021, 11).
692 Attention network forecasts time-to-failure in laboratory shear experiments. *Journal*
693 *of Geophysical Research: Solid Earth*, *126*. doi: 10.1029/2021JB022195
- 694 Johnson, C. W., & Johnson, P. A. (2021). Learning the low frequency earthquake daily
695 intensity on the central san andreas fault. *Geophysical Research Letters*, *48*(15),
696 e2021GL092951. doi: 10.1029/2021GL092951
- 697 Kaproth, B., & Marone, C. (2013). Slow earthquakes, preseismic velocity changes, and
698 the origin of slow frictional stick-slip . *Science*, *341*(6151), 1229–1232.
- 699 Kufner, S., Brisbourne, A., Smith, A., Hudson, T., Murray, T., Schlegel, R., . . . Lee, I.
700 (2021). Not all icequakes are created equal: Basal icequakes suggest diverse bed
701 deformation mechanisms at Rutford Ice Stream, West Antarctica . *Journal of*
702 *Geophysical Research: Earth Surface*, *126*(3), 1–17.
- 703 Kuperman, W., & Turek, G. (1997). Matched Field Acoustics. *Mechanical Systems and*
704 *Signal Processing*, *11*(1), 141–148.

- 705 Laurenti, L., Tinti, E., Galasso, F., Franco, L., & Marone, C. (2022). Deep learning for
706 laboratory earthquake prediction and autoregressive forecasting of fault zone stress.
707 *Earth and Planetary Science Letters*, 598, 117825. doi:
708 <https://doi.org/10.1016/j.epsl.2022.117825>
- 709 Lipovsky, B., & Dunham, E. (2016). Tremor during ice-strem stick slip . *The Cryosphere*,
710 10, 385–399.
- 711 Lipovsky, B., & Dunham, E. (2017). Slow-slip events on the Whillans Ice Plain,
712 Antarctica, described using rate-and-state friction as an ice stream sliding law . *J.*
713 *Geophys. Res. Earth Surf.*, 122, 973–1003.
- 714 Lipovsky, B., Meyer, C., Zoet, L., McCarthy, C., Hansen, D., Rempel, A., & Gimbert, F.
715 (2019). Glacier sliding, seismicity and sediment entrainment . *Annals of Glaciology*,
716 60(79), 182–192.
- 717 Lundberg, S., & Lee, S. (2017). A unified approach to interpreting model predictions.
718 *Advances in neural information processing systems*, 30.
- 719 Madariaga, R., & Ruiz, S. (2016). Earthquake dynamics on circular faults: A review
720 1970–2015 . *Journal of Seismology*, 20(4), 1235–1252.
- 721 Marone, C. (1998). Laboratory-derived friction laws and their application to seismic
722 faulting . *Annual Review of Earth and Planetary Sciences*, 26(1), 643–696.
- 723 McBrearty, I., Zoet, L., & Anandakrishnan, S. (2020). Basal seismicity of the Northeast
724 Greenland Ice Stream . *Journal of Glaciology*, 1–17.
- 725 Murray, T. (1997). Assessing the paradigm shift: Deformable glacier beds . *Quaternary*
726 *Science Reviews*, 16(9), 995–1016.
- 727 Nanni, U., Gimbert, F., Roux, P., & Lecointre, A. (2021). Observing the subglacial
728 hydrology network and its dynamics with a dense seismic array. *Proceedings of the*
729 *National Academy of Sciences*, 118(28), e2023757118.
- 730 Nanni, U., Gimbert, F., Roux, P., & Lecointre, A. (2022). Dynamic Imaging of Glacier
731 Structures at High-Resolution Using Source Localization With a Dense Seismic
732 Array . *Geophysical Research Letters*, 49, 1–9.
- 733 Nanni, U., Gimbert, F., Vincent, C., Gräff, D., Walter, F., Piard, L., & Moreau, L.
734 (2020). Quantification of seasonal and diurnal dynamics of subglacial channels using
735 seismic observations on an alpine glacier. *The Cryosphere*, 14(5), 1475–1496.
- 736 Pedregosa, F., Varoquaux, G., Gramfort, A., Michel, V., Thirion, B., Grisel, O., ...
737 Duchesnay, E. (2011). Scikit-learn: Machine learning in Python. *Journal of*

- 738 *Machine Learning Research*, 12, 2825–2830.
- 739 Podolskiy, E., & Walter, F. (2016). Cryoseismology . *Reviews of Geophysics*, 54, 708–758.
- 740
- 741 Rabinowicz, E. (1956). Autocorrelation analysis of the sliding process . *Journal of*
- 742 *Applied Physics*, 27, 131–135.
- 743 Ren, C., Peltier, A., Ferrazzini, V., Rouet-Leduc, B., Johnson, P., & Brenguier, F. (2020).
- 744 Machine learning reveals the seismic signature of eruptive behavior at piton de la
- 745 fournaise volcano. *Geophysical research letters*, 47(3), e2019GL085523.
- 746 Ritz, C., Edwards, T., Durand, G., Payne, A., Peyaud, V., & Hindmarsh, R. (2015).
- 747 Potential sea level rise from Antarctic ice sheet instability constrained by
- 748 observations . *Nature*, 528, 115–118.
- 749 Rössli, C., Walter, F., Husen, S., Andrews, L., Lüthi, M., Catania, G., & Kissling, E.
- 750 (2014). Sustained seismic tremors and icequakes detected in the ablation zone of the
- 751 Greenland Ice Sheet . *Journal of Glaciology*, 60(221), 563–575.
- 752 Rouet-LeDuc, B., Hulbert, C., Bolton, D., Ren, C., Riviere, J., Marone, C., . . . Johnson,
- 753 P. (2018). Estimating fault friction from seismic signals in the laboratory .
- 754 *Geophysical Research Letters*, 45, 1321–1329.
- 755 Rouet-LeDuc, B., Hulbert, C., & Johnson, P. (2018). Continuous chatter of the Cascadia
- 756 subduction zone revealed by machine learning . *Nature Geoscience*, 12, 75–79.
- 757 Rubinstein, S., Cohen, G., & Fineberg, J. (2004). Detachment fronts and the onset of
- 758 dynamic friction . *Nature*, 430(2), 1005–1009.
- 759 Scholz, C. (1968). Microfracturing and the inelastic deformation of rock in compression .
- 760 *Journal of Geophysical Research*, 73(4), 1417–1432.
- 761 Schoof, C. (2005). The effect of cavitation on glacier sliding . *Proceedings of the Royal*
- 762 *Society*, 461, 609–627.
- 763 Sergienko, O., MacAyeal, D., & Bindschadler, R. (2009). Stick–slip behavior of ice
- 764 streams: Modeling investigations . *Annals of Glaciology*, 50(52), 87–94.
- 765 Shokouhi, P., Girkar, V., Rivière, J., Shreedharan, S., Marone, C., Giles, C., & Kifer, D.
- 766 (2021, 06). Deep learning can predict laboratory quakes from active source seismic
- 767 data. *Geophysical Research Letters*, 48. doi: 10.1029/2021GL093187
- 768 Shugar, D., Jaquemart, M., Shean, D., Bhushan, S., Upadhyay, K., Sattar, A., . . .
- 769 Westoby, M. (2021). A massive rock and ice avalanche caused the 2021 disaster at
- 770 Chamoli, Indian Himalaya . *Sciences*, 373(6552), 300–306.

- 771 Umlauf, J., & Korn, M. (2019). 3D fluid channel location from noise tremors using
772 matched field processing . *Geophysical Journal International*, *219*(3), 1550–1561.
- 773 Umlauf, J., Lindner, F., Roux, P., Mikesell, D., Haney, M., Korn, M., & Walter, F.
774 (2021). Stick-Slip Tremor Beneath an Alpine Glacier . *Geophysical Research Letters*,
775 *48*, 1–10.
- 776 Vandemeulebrouck, J., Roux, P., Gouédard, P., Legaz, A., Revil, A., Hurst, A., . . .
777 Jardani, A. (2010). Application of acoustic noise and self-potential localization
778 techniques to a buried hydrothermal vent (Waimangu Old Geyser site, New
779 Zealand). *Geophysical Journal International*, *180*, 883–890.
- 780 Vincent, C., & Moreau, L. (2016). Sliding velocity fluctuations and subglacial hydrology
781 over the last two decades on argentière glacier, mont blanc area. *Journal of*
782 *Glaciology*, *62*(235), 805–815. doi: 10.1017/jog.2016.35
- 783 Walter, F., Gräff, D., Lindner, F., Paitz, P., Knöpfl, M., Chmiel, M., & Fichtner, A.
784 (2020). Distributed acoustic sensing of microseismic sources and wave propagation
785 in glaciated terrain . *Nature Communications*, *11*(2436), 1–10.
- 786 Walter, F., Roux, P., Rössli, C., Lecointre, A., Kilb, D., & Roux, P. (2015). Using glacier
787 seismicity for phase velocity measurements and Green’s function retrieval.
788 *Geophysical Journal International*, *201*, 1722–1737.
- 789 Wang, K., Johnson, C. W., Bennett, K. C., & Johnson, P. A. (2021, 12). Predicting fault
790 slip via transfer learning. *Nature Communications*, *12*. doi:
791 10.1038/s41467-021-27553-5
- 792 Wang, K., Johnson, C. W., Bennett, K. C., & Johnson, P. A. (2022). Predicting future
793 laboratory fault friction through deep learning transformer models. *Geophysical*
794 *Research Letters*, *49*(19), e2022GL098233. doi:
795 <https://doi.org/10.1029/2022GL098233>
- 796 Weertman, J. (1957). On the sliding of Glaciers . *Journal of Glaciology*, *21*(3), 33–38.
- 797 Winberry, J., Anandakrishnan, S., & Wiens, D. (2011). Dynamics of stick-slip motion,
798 Whillans Ice Stream, Antarctica . *Earth and Planet, Sci. Lett.*, *305*, 283–289.
- 799 Zoet, L., & Iverson, N. (2020). A slip law for glaciers on deformable beds . *Science*,
800 *368*(6486), 76–78.